drones

MDPI

Article

A Multi-Sensor UAV Platform: Design, Testing, and Application for High-Throughput Plant Phenotyping

Liyike Ji [1,2], Xu Wang [1,2,*], Hani Hassan [1,3] and Zhanao Deng [1,4]

[1] Gulf Coast Research and Education Center, Institute of Food and Agricultural Sciences, University of Florida, Wimauma, FL 33598, USA; liyikeji@ufl.edu (L.J.)
[2] Department of Agricultural and Biological Engineering, Institute of Food and Agricultural Sciences, University of Florida, Gainesville, FL 32611, USA
[3] Plant Breeding Graduate Program, Institute of Food and Agricultural Sciences, University of Florida, Gainesville, FL 32611, USA
[4] Horticultural Sciences Department, Institute of Food and Agricultural Sciences, University of Florida, Gainesville, FL 32611, USA
* Correspondence: xuwang1@ufl.edu

Highlights

What are the main findings?

- A regulation-compliant UAV platform with a modular multi-sensor payload (RGB, multispectral, and thermal) was developed for high-throughput plant phenotyping.
- UAV-derived canopy traits (height, coverage, and temperature) showed strong agreement with ground measurements, demonstrating high accuracy for phenotyping applications.

What are the implications of the main findings?

- The modular open-architecture design enables flexible sensor integration and upgrades without reliance on restricted UAV ecosystems.
- The platform provides a reproducible and cost-effective solution for sustainable UAV-based phenotyping in publicly funded agricultural research.

Abstract

Unmanned aerial vehicles (UAVs) are broadly used for high-throughput plant phenotyping, yet their long-term use in public-sector research is increasingly challenged by regulatory restrictions and reliance on proprietary platforms. This study presented a regulation-compliant, modular multi-sensor unmanned aerial system (UAS) designed to deliver flexible, high-quality phenotyping data without dependence on restricted ecosystems. A dual-mount, open-architecture payload integrated RGB, multispectral, and thermal sensors, enabling simultaneous acquisition of structural, spectral, and thermal information within a unified workflow. Field validation in a lantana (*Lantana camara*) breeding trial demonstrated high-precision multi-sensor data fusion and reliable trait extraction. Spatial co-registration achieved centimeter-level accuracy, with alignment errors of 0.88 cm (multispectral) and 3.23 cm (thermal) relative to the RGB reference. UAV-derived canopy height closely matched ground measurements (R^2 up to 0.98; RMSE as low as 1.57 cm), while canopy coverage estimates showed consistency across sensing modalities (R^2 = 0.99; RMSE = 0.02 m^2). Calibrated thermal orthomosaics provided robust canopy temperature estimation (RMSE = 3.13 °C), supporting a quantitative assessment of plant physiological status. Together, these results demonstrate that a regulation-compliant, open-architecture UAV platform can achieve high accuracy in multi-modal phenotyping while maintaining flexibility and cost efficiency. This work demonstrates a scalable and sustainable framework

Academic Editor: Fei Liu

Received: 15 March 2026
Revised: 8 May 2026
Accepted: 11 May 2026
Published: 13 May 2026

for UAV-based phenotyping, enabling researchers to adapt to evolving regulations while advancing data-driven crop improvement.

Keywords: multi-sensor integration; modular payload system; high-throughput phenotyping; aerial imaging; canopy trait extraction

1. Introduction

High-throughput plant phenotyping refers to the rapid, non-destructive quantification of plant traits, including morphological, physiological, and biochemical characteristics, across large populations, with the goal of accelerating crop improvement and breeding decisions. Unmanned aerial vehicles (UAVs) have rapidly evolved into critical tools for precision agriculture, particularly in high-throughput plant phenotyping. Over the past decade, UAV platforms equipped with diverse sensors have enabled rapid, non-destructive, and high-resolution assessment of plant traits across large field trials, with applications spanning stress detection in soybean and other crops [1], nutrient monitoring such as leaf nitrogen content estimation through multi-sensor fusion [2], soil moisture mapping for irrigation management [3], biomass and canopy structure analysis [1], weed detection through multi-sensor fusion [4], and yield prediction in wheat and oilseed rape using multi-temporal and multi-sensor data integration [5,6]. Collectively, these studies highlight the versatility and growing importance of UAV-based approaches in agricultural monitoring and high-throughput phenotyping. Advances in multi-sensor integration and machine learning have further expanded the analytical power of UAV remote sensing by enabling the fusion of spectral, structural, and thermal data streams to improve predictive accuracy in yield estimation and stress diagnostics [7–10]. An early review of UAV applications in precision agriculture highlighted the potential of multi-sensor approaches for drought stress detection, pathogen monitoring, nutrient assessment, and yield prediction, but also noted that routine adoption requires more standardized platforms and streamlined processing pipelines [11].

Despite the rapid growth of UAV-based plant phenotyping, the majority of reported UAV-based multi-sensor phenotyping platforms rely on a few UAV manufactures (e.g., DJI Technology Co., Ltd., Shenzhen, China) [12–17]. These platforms have shown strong capabilities for integrating RGB, multispectral, thermal infrared, LiDAR, and hyperspectral sensors to estimate diverse crop traits, from canopy morphology and nutrient status to yield potential and quality. However, recent United States (U.S.) federal and state-level regulations increasingly restrict the procurement and operation of UAVs manufactured by “covered foreign entities” in federally assisted or state-funded projects, directly affecting the long-term viability of UAV platforms for plant phenotyping [18–20].

For agricultural research programs that depend on long-term, repeatable data collection, these regulatory constraints introduce a critical challenge. UAV platforms are no longer selected solely based on sensor performance or cost efficiency, but also on their eligibility for continued use under public (e.g., federal- or state-approved in the U.S.) funding. As a result, research groups face increased costs, reduced platform continuity, and uncertainty regarding the long-term sustainability of existing UAV-based phenotyping workflows. These conditions further motivate the development of regulation-compliant UAV platforms that can support advanced multi-sensor integration without relying on restricted manufacturers.

Although most UAV-based phenotyping studies have relied on a few restricted UAV manufacturers, studies have demonstrated the feasibility of regulation-compliant UAV

https://doi.org/10.3390/drones10050372

platforms for remote sensing. For example, a custom Vulcan hexacopter equipped with a multispectral and a thermal infrared camera was developed to monitor crop water stress in pomegranate orchards [21]. A Teledyne FLIR SIRAS UAV carrying dual sensors (thermal infrared and RGB) was employed to estimate strawberry canopy volume using deep learning models [22]. Additionally, a WingtraOne fixed-wing UAV equipped with a MicaSense RedEdge multispectral camera has demonstrated effective performance for nitrogen monitoring in winter wheat [23]. Besides the aforementioned UAVs, a growing number of U.S.-manufactured UAVs have been developed, primarily including those on the Department of Defense "Blue UAS" list [24]. While Blue UAS platforms meet stringent security and compliance standards, recent analyses of the current U.S. drone market indicate that many of these systems are optimized for defense rather than agricultural research, often offering limited payload flexibility or higher acquisition costs [21]. Additionally, previous work reviewed evolving UAV regulations (i.e., in the State of Florida, U.S.) and evaluated regulation-compliant UAV options for agricultural imaging and mapping, emphasizing the need for modular, research-oriented platforms that balance compliance, cost, and sensor integration flexibility [25].

Beyond regulatory compliance, a significant barrier to the advancement of high-throughput phenotyping is the "black-box" nature of commercial all-in-one sensor suites. For example, commercial cameras, such as the MicaSense RedEdge/Altum-PT, the FLIR Duo Pro R, and the Sentera Double 4K and 6X series sensors, integrate different types of imaging sensors into a single device to enable multi-sensor data collection in one flight. These proprietary systems often feature rigid, compact designs that sacrifice sensor performance for a small footprint and prevent researchers from upgrading individual components as newer technologies emerge, thereby forcing the costly purchase of redundant systems when a single sensor modality becomes obsolete. Additionally, commercially available multi-sensor solutions for UAV remote sensing remain scarce. Customized integrations, such as the GRYFN system (U.S.), represent a reliable solution but are typically offered as complete turnkey solutions rather than modular platforms that researchers can configure independently [26]. A carefully designed multi-sensor integration solution with a regulation-compliant UAV platform will be a desirable and sustainable approach to achieve optimal performance in UAV-based remote sensing.

In this study, we explore a practical approach to these combined regulatory and sensor integration challenges by developing and validating a modular, regulation-compliant multi-sensor UAV platform designed specifically for high-throughput plant phenotyping. By leveraging the expanded payload capacity of a mid-lift UAV, we decouple sensing, power distribution, and onboard computing across independent mounting surfaces, enabling flexible integration of research-grade sensors without reliance on proprietary ecosystems. The key contributions of this work are as follows. First, we demonstrate a regulation-compliant UAV platform based on the Inspired Flight IF800 that supports integrated multi-sensor phenotyping, addressing current regulatory constraints affecting publicly funded research. Second, we implement a modular payload integration approach that enables independent integration and upgrading of RGB, multispectral, and thermal sensors, overcoming the limitations of proprietary closed-system designs. Third, we establish an end-to-end, reproducible workflow for multi-sensor data acquisition, co-registration, and plant-level trait extraction. Finally, we validate the system in a real breeding trial, demonstrating that a regulation-compliant platform can achieve phenotyping accuracy while maintaining flexibility and cost efficiency. By providing a reproducible, cost-effective, and adaptable reference design, this work aims to support sustainable, regulation-compliant UAV phenotyping infrastructure for publicly funded agricultural research projects.

2. Materials and Methods

2.1. Regulation-Compliant UAV Selection

The integration work was conducted using the Inspired Flight IF800 TOMCAT Quadcopter (Inspired Flight Technologies, San Luis Obispo, CA, USA) (Figure 1), a regulation-approved UAV that meets U.S. compliance requirements for public-sector research. This platform was selected based on: (1) mid-level payload capacity that allows multiple sensing units onboard, (2) long flight endurance (i.e., 54 min without payload, and (3) acceptable cost (Table 1; approximately $22,000 base price as of early 2025), which is lower than or comparable to many research-grade UAV platforms with similar payload capacity and regulatory compliance [25], which together make it suitable for agricultural remote sensing.

Figure 1. Inspired Flight IF800 Quadcopter with dovetail payload interface.

Table 1. Key specifications of the Inspired Flight IF800.

Flight Duration Without Payload (min)	Empty Weight	Max Payload Capacity	Max Gross Takeoff Weight	Max Flight Speed (m s^{-1})	Base Price (Approx.)	Sensor Integrated	External Payload
54	4.2 kg/ 9.2 lb	3.0 kg/6.6 lb	11.5 kg/25.3 lb	22	$22K	No	Yes

Prices listed are estimates based on base configurations as of early 2025 and may vary depending on specific configurations and vendors.

2.2. Multi-Sensor Payload Integration

Building upon the IF800 platform described above, a key feature enabling multi-sensor integration is its dovetail quick-release connector, which provides a standardized, secure, and tool-free interface for mounting external payloads. This design ensures secure attachment, rapid field deployment (i.e., quick installation, removal, and interchange of payload components in field conditions without specialized tools), and straightforward interchangeability across missions. The dovetail assembly can also support power delivery and communication with payloads, enabling the streamlined integration of sensors and peripherals. In this study, however, the dovetail was employed solely as a mechanical fixture. Power supply and data transfer for the onboard payloads were managed separately to accommodate the distinct requirements of each component.

For multi-sensor payloads mounted on the IF800, one practical approach is to attach a gimbal unit to the dovetail connector and integrate multiple sensors on the gimbal. Although this configuration is generally reliable, it incurs additional cost and is constrained by the gimbal's limited capacity to accommodate more than one sensor. Furthermore, operating the gimbal increases the power demand on the drone, thereby reducing flight duration. These challenges highlight the relative novelty of the design in this case study, due to the lack of established reference designs tailored for UAV-based remote sensing applications.

To address these limitations, we designed a customized payload integration system capable of supporting multiple sensors (Figure 2). The payload integration system consisted of two components designed to maximize stability, modularity, and compatibility with the IF800 UAV. The first was a dovetail-mounted bracket that could be attached directly to the dovetail connector, allowing sensors to be easily assembled or disassembled as needed. The bracket was arranged in a forward-facing orientation and incorporated a fixed tilt, which was adopted based on commonly used configurations in commercial UAV payload mounting systems and further adjusted to compensate for UAV pitch during flight and maintain a near-nadir sensor orientation (Figure 3). The mount did not require an external power supply and could accommodate up to three sensing units in small sizes. In this project, we adopted an RGB camera (LUMIX DMC-LX10, Panasonic, Osaka, Japan), a multispectral camera (RedEdge-P, MicaSense, Seattle, WA, USA), and a thermal infrared camera (ICI 8640P, Infrared Cameras Inc., Beaumont, TX, USA). While this mount was not optimized for sensors requiring high-speed and high-precision motion control, such as LiDAR, it was well-suited for remote sensing applications involving imaging sensors and photogrammetry-based mapping. Moreover, the design was compatible with other UAV platforms that are equipped with the same dovetail connector, ensuring versatility and broader applicability.

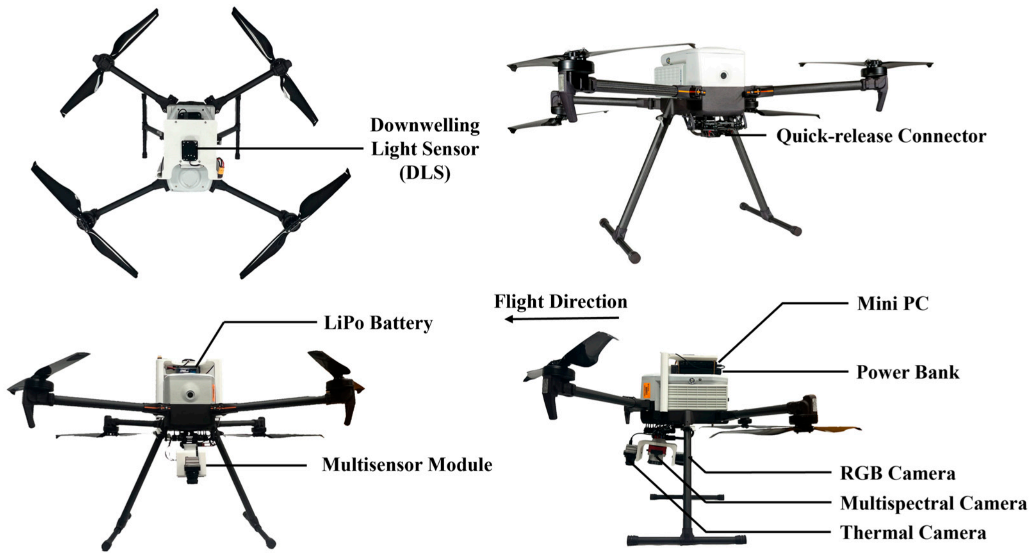

Figure 2. Multiple views of an IF800-based UAS with a multi-sensor payload. The quick-release connector allows secure, interchangeable installation of RGB, multispectral, and thermal sensors.

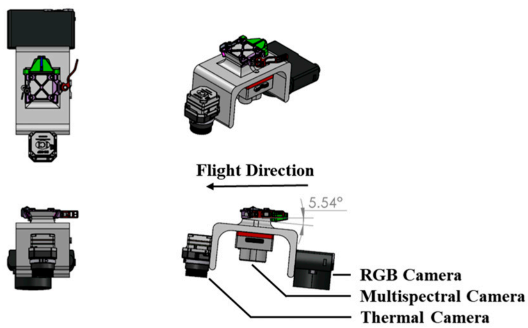

Figure 3. Multiple views of the pitch-compensating payload bracket.

The bracket incorporates a fixed tilt of 5.54°, which was adopted based on commonly used configurations in commercial UAV payload mounting systems and further adjusted to match the flight characteristics of the IF800 platform. This tilt compensates for forward UAV pitch during flight and maintains a near-nadir sensor orientation.

The second component was a platform extended above the UAV body (Figure 4), leaving clearance between its underside and the UAV body's top surface. This configuration allowed additional equipment to be mounted on both the upper and lower surfaces of the platform. In this project, two external power sources, a downwelling light sensor (DLS, MicaSense, Seattle, WA, USA), and an onboard mini-personal computer (mini-PC, Quieter 4C, MeLE, Shenzhen, China) for camera control and data storage were attached to this platform. There were also two channels that extended from the platform and aligned with the UAV body's side frame. These channels were specifically designed to protect the power and control cables linking the equipment attached to the platform with the sensors mounted on the bracket. Key details of the integrated sensors and the onboard equipment are summarized (Table 2). Detailed specifications of the custom dovetail-mounted bracket and the raised top platform are summarized (Table 3). Reported parameters include fabrication method and material, overall dimensions, component mass, mounting interfaces, and cable-management features. A SolidWorks (v2025, Dassault Systèmes, Waltham, MA, USA) file (in STEP format) illustrating the design of the two components is provided in the Supplementary Materials.

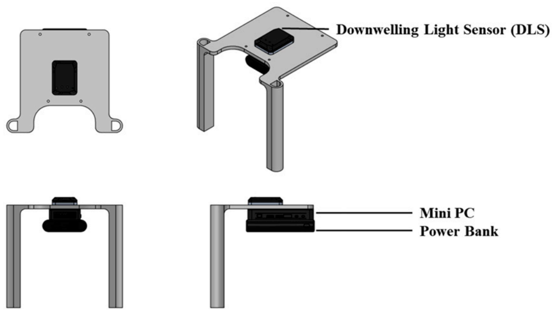

Figure 4. Multiple views of the custom-designed top platform mounted on the IF800 UAV.

Table 2. Specifications of integrated sensors and an onboard computer.

Sensor Type	Sensor Name	Key Specs	Usage	Advantages
RGB	Panasonic LUMIX LX10	20.1 MP; Visual Spectrum	General imaging and mapping	High-res, cost-effective camera for visual documentation and mapping
Multispectral	MicaSense RedEdge-P	1.6 MP each of: Blue (475 nm), Green (560 nm), Red (668 nm), Red Edge (717 nm), NIR (842 nm); 2 cm Ground Sampling Distance (GSD) at 60 m	Vegetation index and crop monitoring	Enables 50 + vegetation indices; ideal for crop health and phenotyping studies
Thermal	ICI 8640P	640 × 512 px; LWIR (7–14 µm); accuracy: ±1 °C	Temperature for biotic and abiotic stress evaluation	High accuracy and resolution; detects subtle temperature differences in plants
Onboard computer	Quieter 4C, MeLE Mini PC	Quad-core Intel CPU; 16 GB RAM; 512 GB SSD	Real-time data sync and storage	Compact, lightweight; suitable for UAV integration

Table 3. Specifications of the custom payload bracket and top platform.

Category	Dovetail-Mounted Pitch-Compensating Bracket	Raised Top Platform (Electronics/Power)
Primary function	Nadir mounting of sensors	Mounting of auxiliary electronics and power modules
Fabrication method	FDM 3D printing	FDM 3D printing
Material	PETG	PETG
Mass (printed part only)	172 g	228 g
Dimensions (X × Y × Z bounding box) *	85.0 × 101.2 × 135.0 mm	214.0 × 190.0 × 190.0 mm
UAV attachment interface	IF800 dovetail quick-release	Screw-mounted
Pitch compensation	5.54° fixed tilt	/
Mounting capacity	Up to 3 sensors (modifiable)	Upper and lower surfaces
Cable management	External routing	Integrated dual side channels for cable protection
Demonstrated payload in this study	RGB camera 312 g; multispectral camera + DLS 363 g; thermal camera 72 g	Power bank 414 g; mini-PC 228 g; LiPo battery 8 g (plus accessories)
Print settings (key parameters)	0.2 mm layer height; 0.4 mm line width; 2 walls; 40% cubic infill; 210 °C nozzle/60 °C bed	

* Dimensions reported as slicer-derived model bounding box (X, Y, Z).

2.3. Power Supply and Data Transmission Design

In this project, the dovetail connector functioned solely as a mechanical interface. All power supply and data transmission were instead managed through a custom wiring scheme independent of the UAV's onboard power and control system. The digital RGB camera operated on its internal battery, while the multispectral camera was powered by an external LiPo battery (Zeee, 11.1v, Dongguan, China). The thermal infrared camera received power via the mini-PC's USB port, while the mini-PC was powered by an external power bank (Figure 4). This independent power supply design minimized the drain on the UAV's power system, thereby extending flight duration (Table 4).

Table 4. Power management for integrated sensors and a computing unit.

Sensor Type	Power Source	Delivery Method/Notes
RGB camera	Internal battery (built-in)	Operates independently; no external wiring required
Multispectral camera	External lithium polymer battery (Zeee, 50C, 11.1 V, 24.42 Wh)	Mounted alongside the payload; provides stable endurance for imaging
Thermal camera	Indirectly powered via mini-PC + power bank	USB-C from power bank → mini-PC → thermal camera (USB-A to Mini-USB)
Mini-PC	High-capacity power bank (20,000 mAh, 144.78 × 28.45 × 74.42 mm)	Dedicated supply for onboard processing; ensures stable power for long missions

Regarding sensor control and data transfer (Figure 5), the digital and multispectral cameras captured images at one-second intervals by their built-in intervalometers, with images stored directly on their internal memory cards. The thermal infrared camera was configured with a trigger interval of 0.2 s and controlled by IRFlashPro software (Infrared Cameras Inc., Beaumont, TX, USA; https://buy.infraredcameras.com/products/ir-flash-pro-annual-subscription, accessed on 11 May 2026) running on the mini-PC, with images stored on the computer's internal drive. In practice, this resulted in an effective acquisition rate of approximately 3–4 frames per second. This configuration allowed each camera to operate independently without requiring central synchronization, as the different image types (RGB, multispectral, and thermal) would be processed separately to generate distinct field orthophotos.

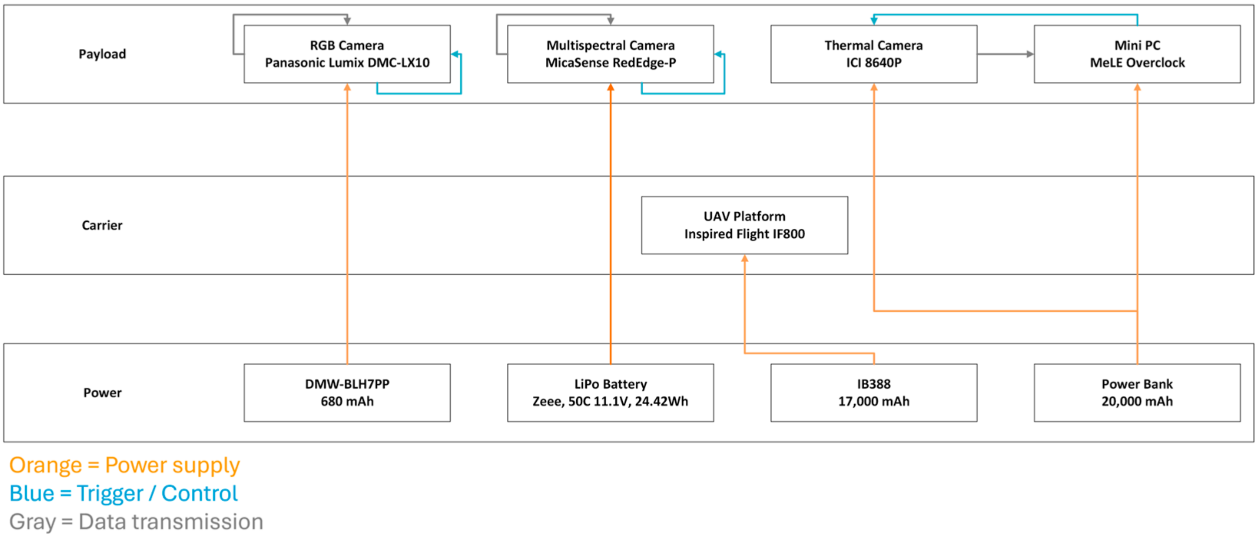

Figure 5. Power supply and data transmission schematic of the multi-sensor payload. Orange arrows indicate power supply connections, blue arrows indicate trigger/control signals, and gray arrows indicate data transmission.

2.4. *Unmanned Aerial System-Based Field Data Collection*

The unmanned aerial system (UAS) was validated through a field data collection experiment conducted on a flowering shrub lantana (*Lantana camara*) breeding trial. The field trial was established in March 2025 at the University of Florida Institute of Food and Agricultural Sciences (UF | IFAS) Gulf Coast Research and Education Center (GCREC) in Wimauma, Florida (27°45′15.21″ N, 82°13′43.98″ W). Given the sandy soil composition and annual production system typical of central Florida, the site is characterized by coarse-textured sandy soils with low organic matter content and high drainage capacity, which are commonly managed using raised-bed production systems with plastic mulch to improve water and nutrient retention [27]. Lantana plants were transplanted from nurseries into three raised beds, each about 100 m long. The beds were fumigated and covered with white plastic mulch to optimize growing conditions. The breeding trial encompassed 33 lantana genotypes, including both experimental lines and commercial varieties, selected to represent a wide range of canopy structures and phenotypic variability. These genotypes were used to evaluate the robustness of the UAV-based phenotyping system across diverse plant architectures rather than for genotype-specific analysis. Plants were positioned along the center of each bed with approximately 1.2 m spacing between individuals. At the time of UAV data acquisition, plants were at the flowering stage with a fully developed canopy structure.

UAV image acquisition followed a set of standard operating procedures [28]. Flights were conducted between 11 a.m. and 12 p.m. on 24 June 2025, under clear sky conditions. This acquisition window and weather condition were selected to minimize variability in ambient thermal radiation and illumination across the dataset. The aerial image overlap rate between two geospatially adjacent images was set to 80%, both sequentially and laterally, to ensure optimal orthomosaic photo stitching quality. To achieve the overlaps, considering the shooting frequency and field of view of all three cameras, flight altitude was set at 20 m above the ground level (AGL) with a flight speed of 2 m s^{-1}. The selection of these flight parameters was defined by the specific field-of-view (FOV) and triggering frequency constraints of the thermal sensor to ensure 80% overlap across all imaging modalities. To ensure geospatial accuracy, six ground control points (GCP, 0.6 m $\times$ 0.6 m) were distributed evenly around the trial perimeter and surveyed by a Global Navigation Satellite Systems (GNSS) receiver (Reach RS2, Emlid, Budapest, Hungary), providing centimeter-level spatial accuracy for subsequent georeferencing of all imagery.

For raw image calibration, multiple sensor-specific targets (Figure 6) were positioned within the field of view during each mission. For RGB imaging, a color reference chart (Spyder Checkr 24, Datacolor, Lawrenceville, NJ, USA) was photographed before and after flights to standardize color balance. For multispectral imaging with the MicaSense RedEdge-P camera, a reflectance panel (MicaSense, USA) was imaged pre- and post-flight, and the downwelling light sensor (DLS, MicaSense, USA) mounted above the UAV recorded incident light conditions throughout each mission. For thermal imaging, the thermal camera lens was manually adjusted before takeoff to achieve proper focus at the operational flight altitude. The imaging distance was entered into the IRFlashPro software to ensure accurate radiometric conversion. Four reference targets were placed in the field: a black-painted aluminum sheet, a white-painted aluminum sheet, a wooden panel, and ice–water mixture in an insulated container. These materials provided a wide radiometric range for validating pixel-based temperature retrievals. To capture thermal reference targets imagery, the UAS was hovered at the operational flight altitude for 30 s before and after the main image acquisition flight over the breeding trial.

Figure 6. Sensor-specific calibration targets used for image radiometric and reflectance correction, including RGB color checker, multispectral reflectance panel, and thermal reference targets. The thermal references include a black-painted aluminum sheet, a white-painted aluminum sheet, a wooden panel, and an ice–water mixture in an insulated container, representing surfaces with different emissivities and temperatures for thermal calibration.

2.5. Ground Truth Data Collection

Ground truth measurements were collected to validate key plant traits derived from images. Canopy height was measured manually in 30 representative plants using a tape measure from the mulch surface to the highest leaf tip. The 30 plants used for ground validation were selected by the breeding team as representative individuals spanning the observed range of canopy sizes and architectures in the trial. Canopy temperature was recorded for the same 30 plants before and after flights using a handheld infrared thermometer (Extech IR400, Extech Instruments, Nashua, NH, USA). Each plant was measured three times and averaged to minimize operator variability. These ground observations were compared with UAV-derived traits for subsequent evaluation.

2.6. Digital Trait Extraction for Validation

An integrated data processing pipeline was developed to extract digital traits from aerial images (Figure 7). The workflow included raw image calibration, orthomosaic field map generation, plant segmentation, and plant-level phenotypic trait extraction. All image processing and analysis were conducted using a combination of commercial and open-source software provided in the corresponding subsections below. All image processing was performed on a workstation equipped with a multi-core CPU (24 cores) and 512 GB RAM.

2.7. RGB Image Pre-Processing

Raw RGB images from the digital camera were imported into Adobe Lightroom (Adobe, San Jose, CA, USA) for batch processing. Lens geometry correction was performed using the application's automatic profile correction feature, effectively removing residual distortion without manual adjustment. Color standardization was achieved by applying a color profile derived from frames containing the SpyderCHECKR 24 reference chart, ensuring consistent white balance and color balance across the entire mission. All corrected images were exported as 16-bit TIFF files for downstream photogrammetry and trait extraction (Figure 7 and Table 5).

Table 5. Data management configuration of integrated sensors and computing unit.

Component	Data Storage	Capture Interval	Control Method/Notes
RGB camera	Internal SD card	1 s	Auto-timed capture; images stored directly to an SD card
Multispectral camera	CFexpress card	1 s	Triggered via MicaSense web interface (Wi-Fi); interval configurable by user
Thermal camera	Mini-PC (SSD)	~0.2 s	Triggered via IRFlashPro software on mini-PC; high-frequency thermal logging
Mini-PC	Internal SSD	Continuous logging	Acts as a central hub; stores synchronized thermal data and auxiliary inputs

2.8. Multispectral Image Pre-Processing

Multispectral images from the MicaSense Rededge-P camera were processed in Agisoft Metashape (Version 1.8.4, Agisoft, St. Petersburg, Russia) following a standardized radiometric calibration workflow [28], including: (i) reflectance correction using images of a calibrated reflectance panel captured before and after each flight, (ii) illumination normalization using measurements from the onboard downwelling light sensor (DLS), and (iii) correction for sensor-specific optical effects, including vignetting and band alignment. These calibrated images were subsequently used for image alignment and orthomosaic generation as described in Section 2.10.

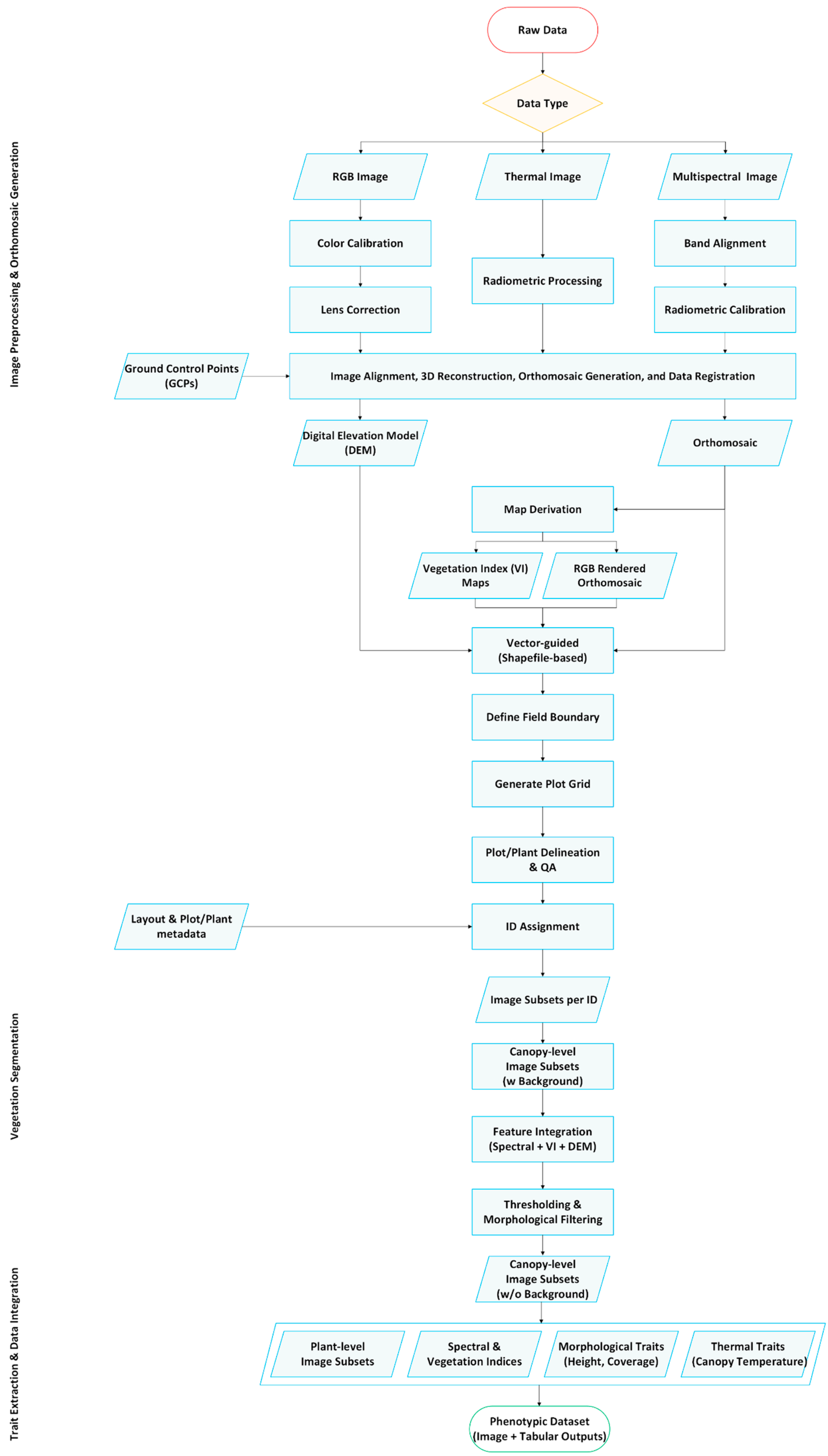

Figure 7. End-to-end workflow for UAV multi-sensor data pre-processing and trait extraction.

2.9. Thermal Image Pre-Processing

Thermal images were recorded as radiometric JPEG files during flight under consistent acquisition conditions, including fixed flight altitude and camera settings, and a short mission duration around solar noon under clear sky conditions to minimize environmental variability. Raw thermal data were processed following the manufacturer's recommended radiometric calibration procedures using IRFlashPro software (Infrared Cameras Inc., USA). Radiometric JPEG images were converted to 16-bit TIFF format using embedded metadata, preserving per-pixel temperature information for subsequent analysis (Figure 7 and Table 5). To account for environmental influences on thermal measurements (e.g., ambient temperature, surface emissivity, and solar radiation), in-field reference targets with known temperatures were used for radiometric calibration. Mean pixel values extracted from these targets were regressed against corresponding ground-measured temperatures to establish a calibration model, which was subsequently applied to convert pixel intensities into canopy temperature values. This approach improves the reliability and comparability of thermal measurements under field conditions.

Four thermal reference targets were selected to span a broad radiometric range under field conditions: a black-painted aluminum sheet (high absorptivity), a white-painted aluminum sheet (high reflectivity), a wooden panel (intermediate emissivity), and an ice–water mixture (~0 °C reference). Surface temperatures of each target were measured using a handheld infrared thermometer immediately before and after UAV flight. For each reference target, a region of interest (ROI) was manually delineated in the thermal orthomosaic (i.e., areas marked by blue dashed lines, Figure 8), and all contained pixels were extracted to compute the mean pixel intensity. The four targets spanned a temperature range of approximately 0–55 °C, enabling regression calibration across a broad radiometric spectrum. These calibration procedures collectively reduce the influence of ambient environmental conditions and improve the reliability and comparability of thermal measurements across the dataset.

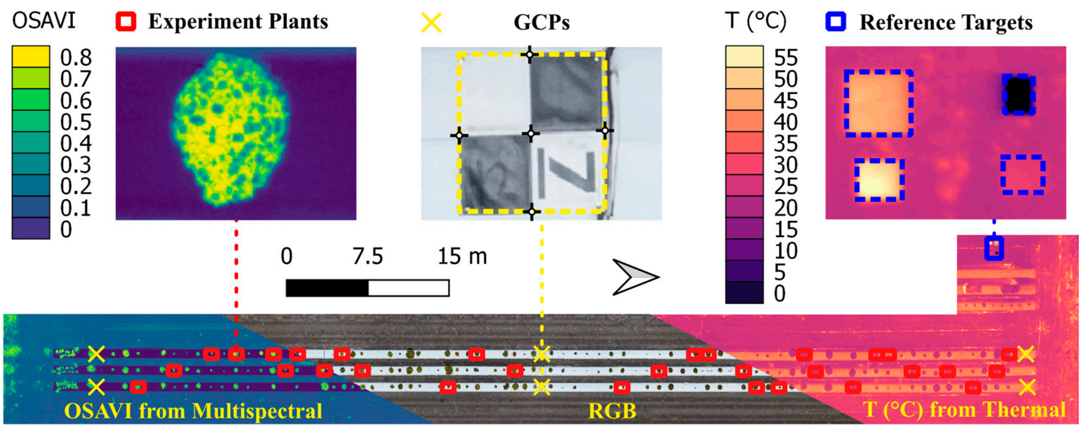

Figure 8. Co-registered RGB, multispectral, and thermal orthomosaics aligned with GCPs.

2.10. Orthomosaics Generation

Pre-processed RGB and multispectral images were processed in Agisoft Metashape to generate georeferenced orthomosaics and digital surface models using a structure-from-motion (SfM) photogrammetry pipeline [28]. Thermal radiometric images were processed using the identical workflow to produce a georeferenced thermal orthomosaic; however, due to insufficient resolution, no digital surface model was generated from the thermal data.

During photogrammetric processing, all six GCPs were manually identified and marked in each dataset (RGB, multispectral, and thermal) and used for camera position and orientation optimization and orthomosaic geospatial accuracy improvement. Absolute georeferencing accuracy was quantified using the root mean square error (RMSE) of the GCP residuals reported by Agisoft Metashape. Reprojection error values correspond to the mean pixel reprojection error after GCP incorporation and camera parameter optimization and were reported by Agisoft Metashape as well.

To assess inter-sensor spatial co-registration accuracy, an additional cross-sensor offset analysis was performed using four checkerboard GCP targets located at the field corners (Figure 8). These GCPs were the same targets used during orthomosaic georeferencing. For each corner GCP, five geometrically defined intersection points were selected, including the central intersection and four outer black–white edge intersections (cross markers on the GCP, Figure 8), yielding a total of 20 evaluation checkpoints (four GCPs × five geometrically defined intersection points per target). This configuration ensures consistent feature identification and adequate spatial sampling for evaluating inter-sensor co-registration accuracy. Corresponding intersection points were manually identified in the RGB, multispectral, and thermal orthomosaics. The RGB orthomosaic served as the reference dataset. Horizontal positional offsets between matched intersections were quantified in QGIS (QGIS.org, Grüt, Switzerland).

2.11. Plant Segmentation

To derive plant-level traits, orthomosaics from RGB, multispectral, and thermal imagery were processed using a unified workflow. First, individual plant regions were cropped from each orthomosaic using rectangular plot boundaries defined as polygon shapefiles. These boundaries were calculated based on row corner coordinates and inter-plant spacing, with each boundary linked to a unique plant identifier. The cropped regions contained both canopy pixels and background elements (e.g., plastic mulch as the raised bed's surface and soil). Next, segmentation masks were generated within each cropped region to separate the canopy from the background, followed by trait extraction tailored to each sensor modality.

Canopy masks from the RGB orthomosaic were generated using hue-saturation-value (HSV) thresholding. Each raw plant-level RGB orthomosaic was first converted into three 8-bit grayscale channels (H, S, and V). Threshold values were then applied to each channel: Hue values between 20 and 90, Saturation values between 21 and 210, and Value values between 9 and 254. Pixels satisfying all three threshold conditions were classified as vegetation to create the binary canopy mask.

Canopy masks from multispectral orthomosaics were generated using a three-step spectral-structural segmentation approach. First, the five-band multispectral orthomosaic was converted to an optimized soil-adjusted vegetation index (OSAVI [29]; Equation (1)) orthomosaic, which was selected due to its reduced sensitivity to soil background reflectance and improved performance under partial canopy cover conditions compared to conventional indices such as NDVI. Pixels with OSAVI values greater than or equal to 0.6 were classified as vegetation to create an initial binary canopy mask. This threshold was selected to suppress soil background while retaining dense canopy pixels. Second, the digital elevation model (DEM) for each plant was normalized to an 8-bit (0–255) grayscale image to standardize elevation distributions across plants. The normalized elevation values were then partitioned using CKMeans clustering (k = 3) [30], which separates pixels into low- (soil between raised beds), intermediate- (raised bed surface), and high-elevation groups (plant canopies). The threshold defining canopy pixels was set as the centroid of the intermediate cluster, representing the transition between ground surface and elevated vegetation. Pixels with elevation values greater than or equal to this threshold were classified as canopy. When CKMeans clustering failed due to insufficient valid pixels, the threshold was approximated using the 66th percentile of normalized elevation values. Finally, the refined canopy mask was obtained by computing the pixel-wise intersection between the OSAVI-derived spectral mask and the DEM-derived structural mask, retaining only pixels simultaneously identified as vegetated and structurally elevated. This combined approach reduced soil and shadow misclassification while preserving canopy integrity across heterogeneous field conditions.

$$\text{OSAVI} = \frac{(\text{NIR} - \text{Red})}{(\text{NIR} + \text{Red} + 0.16)} \times (1 + 0.16), \tag{1}$$

where NIR and Red represent the near-infrared and red band reflectance values, respectively, and 0.16 is the soil adjustment factor.

Since the thermal, RGB, and multispectral orthomosaics were co-registered using identical GCPs, the high-fidelity canopy masks derived from the RGB or multispectral data could be used to define corresponding regions in the thermal imagery. In this study, multispectral-derived canopy masks were projected onto the thermal orthomosaic to crop canopy regions. To account for minor spatial offsets and edge effects, the thermal masks were slightly eroded to focus on the central canopy area.

2.12. Phenotypic Trait Extraction

Canopy height was estimated from both RGB- and multispectral-derived digital surface models (DSM) and digital terrain models (DTM). For each plant, DTM was generated from non-vegetated regions corresponding to the mulch surface along the raised beds, while the DSM represented the upper canopy surface. The canopy height for each plant was calculated as the mean of the top 5% of height values within its canopy boundary, corresponding to the difference between DSM and DTM elevations. RGB- and multispectral-based heights were computed separately using their respective canopy masks.

Canopy coverage was derived from both RGB and multispectral orthomosaics using the segmentation masks described in Section 2.11. Coverage was calculated as the total number of canopy pixels within each canopy multiplied by the square of the ground pixel size, which represents the ground area covered by each pixel, allowing conversion from pixel counts to real-world area units. The GSD values were obtained directly from the processing report generated in Agisoft Metashape after orthomosaic construction.

Canopy temperature estimation involved radiometric calibration followed by pixel-wise temperature conversion. Radiometric JPEGs were first converted to 16-bit TIFFs in IRFlashPro, which preserved per-pixel radiometric information. To establish a relationship between pixel intensity and true temperature, four in-field reference targets (black-painted aluminum, white-painted aluminum, wood panel, and ice–water surface) with known surface temperatures were used. For each target, mean pixel intensity values (P) were extracted from the radiometric orthomosaic and regressed against corresponding thermometer-derived temperatures (T) (Equation (2)).

$$\text{T} = 0.0128\text{P} - 112.1, \tag{2}$$

where T (°C) is the estimated canopy temperature, and P is the pixel value from the orthomosaic. This calibration model was subsequently applied to all canopy pixels within each plant's boundary defined as the central canopy region from the segmentation mask, to generate spatially consistent canopy temperature maps. For each plant, canopy temperature was calculated as the mean of the top n% of calibrated pixels' values. To evaluate robustness to shaded areas and background interference, canopy temperature estimates derived from the top 1%, 5%, and 10% of canopy pixels were compared with ground-truth measurements.

https://doi.org/10.3390/drones10050372

2.13. Digital Trait Validation

Ground measurements of canopy height and canopy temperature (Section 2.5) were used as reference data for validating UAV-derived traits. Validation focused on canopy height, canopy coverage, and canopy temperature. Canopy height and canopy temperature were validated against physical ground-truth instruments, whereas canopy coverage was validated through cross-sensor consistency.

For all traits, agreement between UAV-derived estimates and reference measurements was evaluated using ordinary least squares (OLS) linear regression. The accuracy of UAV-derived traits was quantified using the coefficient of determination (R^2) (Equation (3)), root mean square error (RMSE) (Equation (4)), mean absolute error (MAE) (Equation (5)), mean bias (Equation (6)), and maximum absolute deviation (Equation (7)). Regression slope and intercept were also examined to identify systematic bias (e.g., consistent under- or over-estimation) across the observed trait range.

$$R^2 = 1 - \frac{\sum_{i=1}^{n}(y_i - \hat{y}_i)^2}{\sum_{i=1}^{n}(y_i - \overline{y})^2}, \tag{3}$$

$$\mathrm{RMSE} = \sqrt{\frac{1}{n}\sum_{i=1}^{n}(y_i - \hat{y}_i)^2}, \tag{4}$$

$$\mathrm{MAE} = \frac{1}{n}\sum_{i=1}^{n}|y_i - \hat{y}_i|, \tag{5}$$

$$\text{Mean bias} = \frac{1}{n}\sum_{i=1}^{n}(\hat{y}_i - y_i), \tag{6}$$

$$Maximum\ absolute\ deviation = max(|y_i - \hat{y}_i|), \tag{7}$$

where y_i represents the ground-measured value, $\hat{y}_i$ is the UAV-derived estimate, $\overline{y}$ is the mean of ground measurement, and n is the number of plants evaluated.

UAV-derived canopy height from RGB- and multispectral-based models was validated against manual tape measurements collected from the 30 selected plants. Validation was conducted separately for each dataset to assess consistency across imaging modalities. Canopy coverage from RGB orthomosaics (HSV-based segmentation) was compared against canopy coverage derived from multispectral orthomosaics (OSAVI-based segmentation) for the same 30 selected plants.

Thermal validation was conducted in two complementary stages to ensure both sensor-level and orthomosaic-level accuracy. First, canopy temperatures were extracted directly from individual images using IRFlashPro software and compared with handheld infrared thermometer measurements for the same 30 plants on the ground. In this comparison, the four thermal reference targets were included to confirm that the thermal camera captured a wide radiometric range under field conditions and to evaluate systematic offsets between airborne and ground measurements. For each plant and reference target, temperature was averaged across all single-frame thermal images in which the object was fully visible, reducing variability caused by viewing geometry and within-canopy heterogeneity. Second, canopy temperatures extracted from the calibrated thermal orthomosaic (Section 2.12) were compared with the corresponding ground thermometer measurements. This analysis quantified the accuracy of the radiometric calibration model and verified that orthomosaic pixel values could be reliably converted into canopy temperatures suitable for phenotyping.

3. Results

3.1. UAS Data Collection

The multi-sensor UAS completed two flight missions successfully during the field validation experiment (Figure 9). Each flight lasted approximately 13 min, providing complete coverage of the breeding trial (~1000 m^2 or 0.25 acre) at 20 m AGL (Table 6). Although the first battery set had sufficient capacity for both missions, it was replaced with a fully charged battery set between flights to maintain consistent power delivery. The IF800 UAV supports hot swapping, which enables battery replacement without requiring a cold restart. Both flights operated autonomously without requiring manual intervention.

Figure 9. Multi-sensor UAS in operation during field data collection over the flowering shrub (lantana) breeding trial.

Table 6. UAV flight performance and operational metrics.

Metric	Value
Total payload mass	1.80 kg
Flight altitude	20 m
Flight speed	2 m s^{-1}
Land coverage	~1000 m^2 (0.25 acre)
Flight duration	13 min
Image overlap (forward/lateral)	80%/80%

3.2. Orthomosaic Generation and Multi-Sensor Co-Registration Accuracy

The orthomosaics used for validation were generated from aerial imagery acquired during the first flight mission. After georeferencing using the same set of GCPs, the RGB, multispectral, and thermal orthomosaics exhibited consistent spatial alignment (Figure 8). The GSDs were 0.47 cm/pixel for RGB imagery, 0.61 cm/pixel for multispectral imagery, and 1.26 cm/pixel for thermal imagery (Table 7). Following the incorporation of GCPs and camera optimization, within-dataset bundle-adjustment reprojection errors averaged

1.09 pixels for RGB imagery, 0.44 pixels for multispectral imagery, and 0.81 pixels for thermal imagery. Absolute georeferencing accuracy, assessed using GCP residuals, yielded vertical RMSE values of 0.34 cm for RGB orthomosaics, 0.47 cm for multispectral orthomosaics, and 0.70 cm for the thermal orthomosaic. These results confirm centimeter-level positioning accuracy.

Table 7. Multi-sensor mapping quality and co-registration accuracy of the integrated UAS.

Metric	RGB	Multispectral	Thermal
GSD	0.47 cm/pix	0.61 cm/pix	1.26 cm/pix
Number of images captured	736	2544	1483
Reprojection error	1.09 pix	0.44 pix	0.81 pix
Vertical RMSE (GCP residuals)	0.34 cm	0.47 cm	0.70 cm
Spatial alignment error *	/(as reference)	0.88 cm	3.23 cm
Trait estimation RMSE	Height: 2.84 cm	Height: 1.57 cm	Temp: 3.12 °C

* Spatial alignment error computed as the RMSE of horizontal (2D) offsets between corresponding GCP-adjacent feature points in the multispectral/thermal orthomosaics relative to the RGB orthomosaic reference (n = 12 points).

Inter-sensor spatial alignment was further evaluated using 2D RMSE of horizontal offsets between corresponding checkerboard intersection points relative to the RGB orthomosaic reference (Table 7). The mean horizontal alignment bias between RGB and multispectral datasets was 0.54 cm, with a 2D RMSE of 0.88 cm, confirming high spatial correspondence. The thermal dataset exhibited a larger horizontal bias of 2.24 cm relative to the RGB reference, with a 2D RMSE of 3.23 cm, which was potentially due to the lower spatial resolution of individual thermal images, which provided fewer distinctive feature points for alignment during photogrammetric processing. Despite this ~3 cm offset, the displacement remained well within acceptable limits for plant-level trait extraction, as the minimum canopy width in the trial was approximately 30 cm. This ensured that thermal pixels remained within the intended plant boundaries, enabling reliable extraction of canopy temperature.

Reported metrics (Table 7) summarize system-level performance for each sensing modality after orthomosaic generation and georeferencing. Ground sampling distance (GSD) indicates spatial resolution, where smaller values correspond to finer detail. Reprojection error reflects internal photogrammetric consistency, while vertical RMSE (from GCP residuals) represents absolute georeferencing accuracy. Spatial alignment error is reported relative to the RGB orthomosaic as the reference dataset and reflects inter-sensor co-registration accuracy. Trait estimation RMSE indicates the agreement between UAV-derived traits and ground measurements. For all error-based metrics, lower values indicate higher accuracy. Metrics are reported to characterize system performance and are not intended for direct ranking across sensors. Overall, the results demonstrate high-quality photogrammetric reconstruction suitable for plant-level phenotyping. Minor increases in spatial error for the thermal dataset were observed but remained negligible relative to the canopy scale and did not affect downstream trait extraction.

3.3. Plant Segmentation and Canopy Coverage

The RGB- and multispectral-based segmentation masks effectively delineate individual canopies across all plots. RGB-derived HSV masks occasionally expanded beyond plant boundaries, whereas multispectral-derived masks provided sharper vegetation-background separation.

Visual overlays further illustrate typical differences between segmentation outputs (Figure 10). The magenta RGB-derived masks generally covered the canopy more completely, while the yellow multispectral-derived masks were slightly smaller and more conservative around the edges. Both approaches effectively captured the canopy area, and this pattern was consistent across plants of different sizes. Similar behavior was observed when masks were overlaid on both RGB and multispectral orthomosaics, suggesting that these boundary differences primarily reflect variations in segmentation criteria rather than differences in image quality.

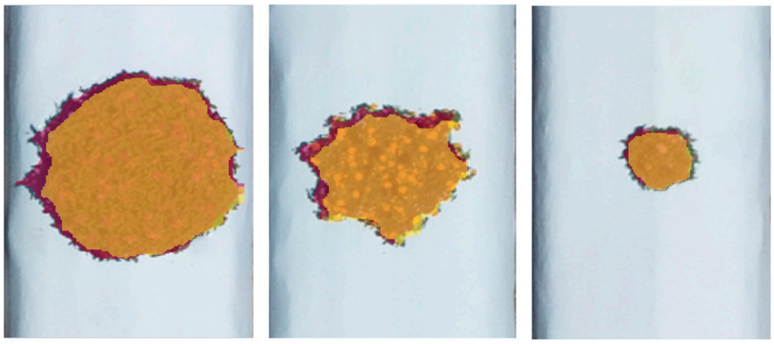

Figure 10. Comparison of canopy segmentation masks overlaid on RGB orthomosaics. Amber: Multispectral mask; Magenta: RGB mask.

To quantitatively assess segmentation performance, canopy coverage from RGB and multispectral masks was compared across plants. The two approaches showed high accuracy (R^2 = 0.99, RMSE = 0.02 m^2; Figure 11), confirming the consistency of canopy delineation between spectral domains. The error distribution ranged from −0.048 to 0.007 m^2, with a mean bias of −0.015 m^2, a maximum absolute deviation of 0.048 m^2, and an MAE of 0.016 m^2.

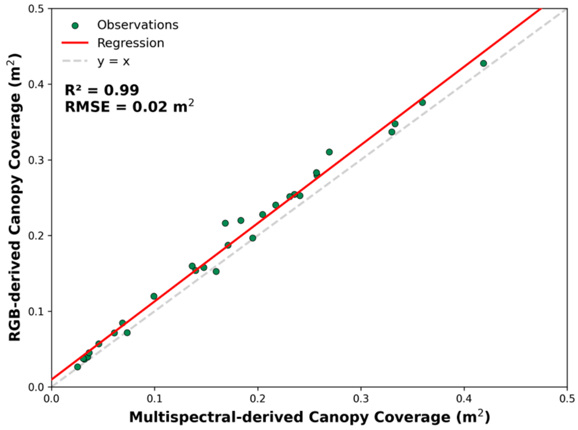

Figure 11. Comparison of canopy coverage derived from RGB- and multispectral-derived masks.

3.4. Canopy Height

Canopy height estimates derived from UAV imagery were highly consistent with ground-measured values. The multispectral-based relative canopy height showed high accuracy compared with manual measurements (R^2 = 0.98, RMSE = 1.57 cm) (Figure 12a). The error distribution ranged from −2.86 to 2.02 cm, with a mean bias of −1.09 cm, a maximum absolute deviation of 2.86 cm, and an MAE of 1.40 cm. Distribution comparisons confirmed close alignment between multispectral-derived and manually measured heights, with slight underestimation at the upper range (Figure 12a).

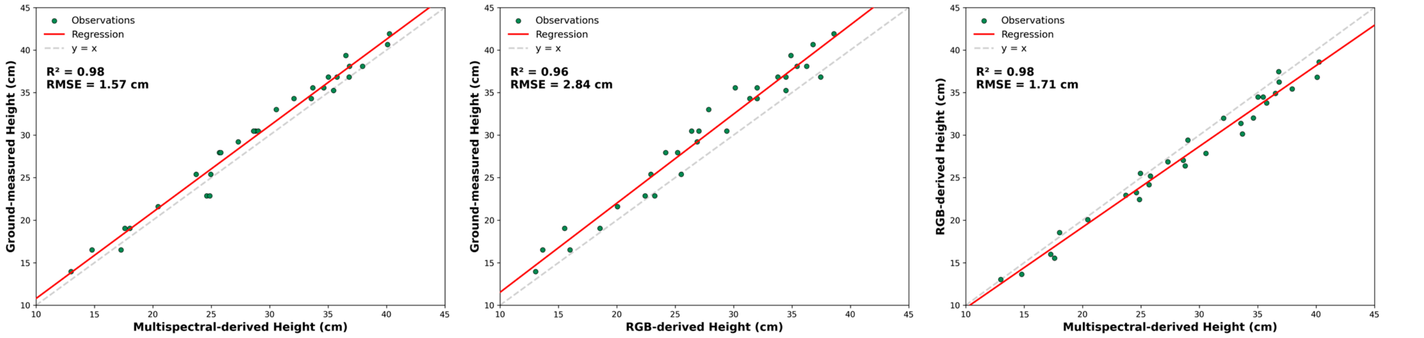

(**a**) (**b**) (**c**)

Figure 12. Accura. assessment of canopy height estimates derived from UAV imagery. (**a**) Comparison between multispectral-derived canopy height and manual measurements; (**b**) Comparison between RGB-derived canopy height and manual measurements, and (**c**) Comparison between multispectral- and RGB-derived canopy heights.

RGB-based relative canopy height also demonstrated strong agreement with ground measurements (R^2 = 0.96, RMSE = 2.84 cm), though with slightly higher variability across plots (Figure 12b). The error distribution ranged from −5.42 to 0.63 cm, with a mean bias of −2.36 cm, a maximum absolute deviation of 5.42 cm, and an MAE of 2.43 cm.

Direct comparison between multispectral- and RGB-derived canopy heights revealed strong inter-sensor consistency (R^2 = 0.98, RMSE = 1.71 cm), confirming the robustness of the photogrammetric workflow across modalities (Figure 12c). The inter-sensor height difference ranged from −0.67 to 3.55 cm, with a mean bias of 1.27 cm, a maximum absolute deviation of 3.55 cm, and an MAE of 1.42 cm.

3.5. Canopy Temperature Validation and Threshold Sensitivity

Sensitivity analysis (Figure 13) demonstrated that canopy temperature estimates remained robust across percentile thresholds. Across the top 1%, 5%, and 10% percentile selections, linear regressions between the radiometric digital numbers derived from the orthomosaics and the ground reference measurements remained remarkably consistent (R^2 = 0.97–0.98; RMSE = 2.72–3.59 °C). While the top 10% threshold yielded a lower RMSE, the gain in explanatory power was negligible, while increasing the potential inclusion of partially shaded foliage or background pixels. Conversely, the top 1% threshold exhibited a higher RMSE, likely due to increased sensitivity to sensor noise and extreme values at the edge of the distribution. The 5% threshold was therefore identified as the optimal sampling density, effectively capturing predominantly sun-exposed canopy surfaces and minimizing the influence of shading or background pixels. Collectively, these results support the use of the 5% criterion as a robust proxy for canopy temperature across diverse thermal environments.

To assess the reliability of UAV-based thermal imagery, canopy temperature estimates were validated using both sensor-level and image-level comparisons (Figure 14). First, canopy temperatures extracted from individual thermal frames in IRFlashPro were compared with handheld infrared thermometer measurements for 30 plants. Four reference targets were additionally included to verify that the thermal camera captured a broad radiometric range under field conditions.

For plant measurements alone (n = 30), regression analysis showed moderate agreement between airborne and ground measurements (R^2 = 0.31, RMSE = 5.18 °C). The error distribution ranged from −8.02 to −3.07 °C, with a mean bias of −5.04 °C and MAE of 5.04 °C, indicating systematic underestimation of canopy temperature by the airborne thermal measurements. These discrepancies were likely attributable to differences in viewing geometry, canopy heterogeneity, and microclimatic variability between airborne observations and handheld measurements. In addition, canopy temperature reflects plant physiological processes such as transpiration and can indicate plant water status. However, thermal indicators may be less sensitive to early stress responses under certain conditions [31], supporting the use of multi-sensor approaches. When reference targets were included (plants + targets, n = 34), regression performance increased substantially (R^2 = 0.98, RMSE = 5.22 °C; Figure 14a), confirming a stable and linear radiometric response across an expanded temperature range.

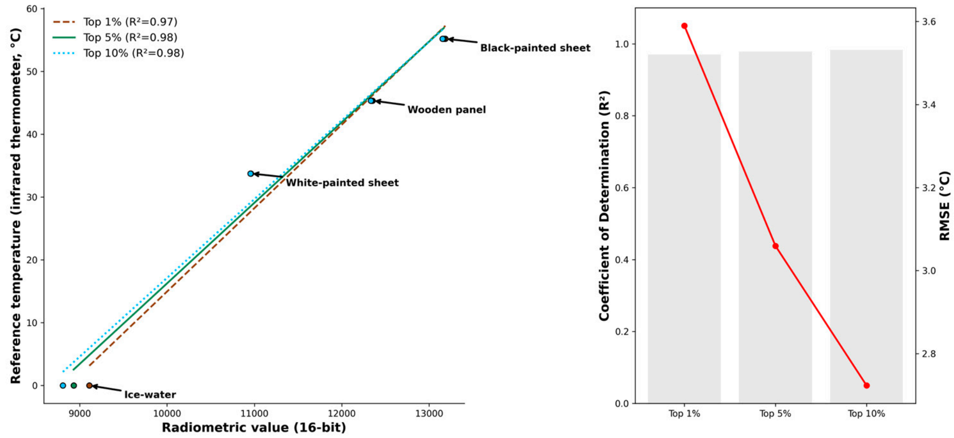

Figure 13. Sensitivity analysis and statistical validation of canopy temperature extraction across percentile thresholds.

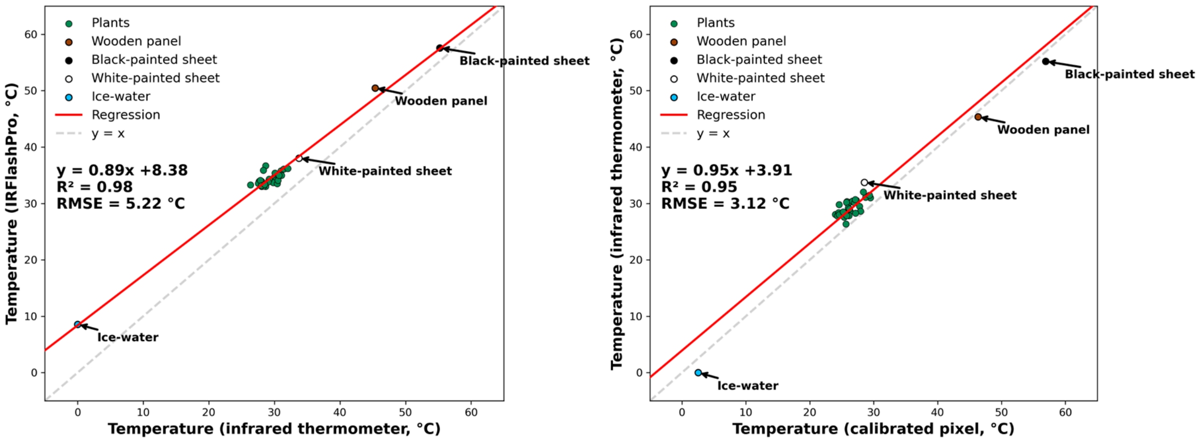

(**a**) (**b**)

Figure 14. Validation of UAV thermal imagery: (**a**) IRFlashPro vs. Infrared Thermometer; (**b**) UAV Orthomosaic vs. Infrared Thermometer.

Next, canopy temperatures derived from the calibrated UAV thermal orthomosaic were compared with corresponding ground thermometer measurements (Figure 14b). For plant measurements alone (n = 30), calibration substantially improved agreement (R^2 = 0.46, RMSE = 3.13 °C). The error distribution ranged from −5.21 to −0.70 °C, with a mean bias of −2.92 °C and MAE of 2.92 °C, indicating a marked reduction in systematic bias following radiometric calibration and orthomosaic processing. When reference targets were incorporated (plants + targets, n = 34), strong linear agreement was observed (R^2 = 0.95, RMSE = 3.12 °C). The comparatively lower R^2 values observed for plant-only datasets were attributable to the limited biological temperature variability among canopies, as the coefficient of determination is strongly influenced by data variance. Despite this, absolute error metrics (RMSE = 3.13 °C; MAE = 2.92 °C) indicate reliable canopy temperature estimation within the agronomically relevant temperature range.

Together, these comparisons confirm that the UAV-mounted thermal camera, when calibrated using in-field reference targets and canopy-focused pixel extraction, provides reliable canopy temperature estimates suitable for quantitative phenotyping applications.

4. Discussion

This study demonstrates a regulation-compliant multi-sensor UAV platform and validates its applicability for high-throughput plant phenotyping through the extraction of canopy structural and thermal traits. Similarly to UAVs paired with off-the-shelf sensors (e.g., DJI ecosystems) and commercial multi-sensor mount solutions (e.g., GRYFN), our platform—a regulation-compliant UAV integrated with research-grade sensors—demonstrated reliable acquisition of co-registered imagery for canopy segmentation, structural trait estimation, and canopy temperature retrieval. While direct performance comparison against commercial systems was not conducted, the observed performance demonstrates that the proposed platform achieves reliable multi-sensor data acquisition suitable for phenotyping applications. To support the cost-effectiveness of the proposed platform, an estimated component-level cost analysis and comparison with representative alternative multi-sensor UAV systems were conducted (Table 8). Cost estimates were compiled using publicly available vendor information current as of February 2026 and are intended to illustrate relative investment requirements rather than exact procurement values. The modular payload design provided flexibility in mounting and replacing sensors, enabling rapid adaptation to different experimental needs. Independent operation of each camera reduced risks of mis-triggering and minimized data transmission bottlenecks. Specifically, the UAV-derived traits (i.e., canopy height and canopy temperature) exhibited high agreement with ground-truth measurements. For traits where direct physical measurement was less feasible, such as canopy coverage, validation was performed through cross-sensor comparison, and the results were consistent. These findings demonstrate that the platform can deliver accurate, multi-modal data within the evaluated breeding trial conditions. The extracted traits provide biologically meaningful indicators of plant performance. Canopy height and canopy coverage reflect structural growth and biomass accumulation, and canopy temperature serves as an indirect indicator of plant water status and stomatal regulation. Together, these traits provide a foundation for assessing plant physiological responses under field conditions. The integration of RGB, multispectral, and thermal sensors provides complementary information by combining structural, spectral, and thermal signals, enabling a more comprehensive assessment of plant status than any single modality alone.

Compared with restricted UAS (e.g., DJI and Autel UAS) reported for agricultural remote sensing, the UAV selected in this study (Inspired Flight IF800) provides a practical balance between payload capacity, endurance, and modular multi-sensor expandability. While custom research airframes (e.g., Vulcan hexacopter) and commercial regulation-compliant systems (e.g., Teledyne FLIR SIRAS) have demonstrated feasibility for remote sensing applications, these platforms are often constrained by either high integration burden, limited multi-sensor flexibility, or reduced adaptability for research-oriented payload development. A broader comparison of regulation-compliant UAV options, including cost, endurance, and payload capacity tradeoffs, has been reviewed [25]. Beyond the adoption of new compliant platforms, the long-term management of existing non-compliant UAV fleets presents an equally pressing operational challenge for publicly funded research programs in the United States. Under current U.S. federal and state regulations, UAVs manufactured by covered foreign entities face hard operational termination without exception or transitional provisions. Affected institutions should proactively plan for the retirement of such fleets, which may include early termination of maintenance contracts and cessation of software update subscriptions, as continued financial investment in non-compliant systems yields no sustainable operational return. Establishing clear fleet transition timelines and budget planning frameworks will be essential for research programs seeking to maintain uninterrupted phenotyping capacity during this regulatory transition period.

Table 8. Estimated component-level cost breakdown and comparison of the proposed modular UAS platform with representative alternative multi-sensor UAV systems (approximate market prices as of February 2026).

Category	This Study (Modular IF800 UAS)	Commercial Integrated System *	Regulation-Compliant Alternative **	Notes
Airframe w/battery	$26,000	$12,000	$37,500	NDAA Compliance
RGB camera	$700	$20,000	$20,375	Replaceable
Multispectral camera	$7500			Same class precision
Thermal camera	$8000			Radiometric
Onboard computing	$400	/	/	Open architecture for Edge AI
Power modules	$60	Included	Included	Independent power
Payload structure	$20	/	/	Customizable
Estimated Total Cost	~$42K	~$32K	~$58K	Approximate values
Upgradeability	High	Low	Medium	Hardware-agnostic
Regulatory compliance	Yes	Often restricted	Yes	Certified

* DJI Matrice 350 RTK + MicaSense Altum-PT. ** FREEFLY Alta X + Sentera 6X Thermal Pro.

The significance of this integration extends beyond mere airframe replacement as it addresses the need for technological sustainability in agricultural research. By enabling multi-sensor phenotyping independent of a single manufacturer's closed ecosystem, this platform provides a pathway for plant phenotyping to maintain high-throughput capabilities as sensor technologies evolve. The modular architecture allows researchers to integrate specialized sensors they already possess and to upgrade individual sensing modalities without replacing the entire payload system, thereby reducing long-term cost and improving adaptability for different plants.

The integration of an onboard mini-PC was a strategic response to the technical limitations observed in standard UAV sensor control modules. Preliminary evaluations of manufacturer-suggested control interfaces revealed instability and low data-transfer rates. These modules also exhibited delayed synchronization workflows after landing, increasing the risk of data loss and reducing operational efficiency. By transitioning to a mini-PC for thermal camera triggering and storage, we ensured immediate data persistence on an internal SSD and eliminated transfer-latency bottlenecks, improving reliability under field conditions. This improvement enhances the reliability of data acquisition, which is critical for maintaining data integrity in high-throughput phenotyping workflows.

Potential drawbacks should also be acknowledged. First, power supplies for sensors were separated from the UAV batteries in this multi-sensor configuration. Although this design preserved the UAV's flight battery capacity and simplified integration across sensors with different voltage requirements, it introduced additional mass and cable routing complexity. Future iterations will implement a unified regulated power distribution system to reduce cabling, improve safety, and simplify deployment. Second, due to the different fields of view across multiple cameras, flight planning is constrained by the smallest field of view to enable image alignment for complete orthomosaic generation across all modalities. The tradeoffs between collecting multi-modal data in a single flight versus collecting each modality in separate flights within a short window should be carefully considered. Third, the system does not provide real-time confirmation of image capture status through the UAV ground station, which could result in incomplete image acquisition due to undetected camera malfunctions during flight. Future work will incorporate sensor status monitoring and error logging. Finally, the 3D-printed PETG mount was designed for three small cameras and was not intended for heavier sensors such as hyperspectral cameras or LiDAR. To expand payload capacity and stiffness, future designs will replace printed structural components with carbon fiber composites or machined aluminum while preserving the modular mounting geometry. In addition, UAV data acquisition is sensitive to environmental conditions (e.g., wind and illumination variability), which may affect image quality across missions. The data processing workflow also requires familiarity with photogrammetry and image analysis, which may present a practical barrier for users without prior experience.

The validation presented here was conducted at a single site within a lantana breeding trial and included a limited ground-truth sample size. Therefore, agronomic generalizability across diverse crop architectures, canopy structures, and environmental conditions were not assessed. Additional multi-site and multi-crop evaluations are required to further quantify robustness and transferability. Additionally, the image processing pipeline developed in this study involved dataset-specific parameter tuning, including HSV thresholding values for canopy segmentation and coefficients for thermal calibration. These parameters were optimized for the lantana breeding trial under the specific imaging and environmental conditions encountered, and their selection and rationale are described in Section 2. The application of this pipeline to other crop species, canopy structures, or environmental conditions will likely require re-parameterization. The open and modular design of the platform is intended to support such adaptation across diverse phenotyping scenarios. Similarly, although the thermal calibration model performed strongly within the evaluated temperature range, broader climatic validation would strengthen the assessment of seasonal transferability. In addition, this study focused on system validation rather than comprehensive biological interpretation or genotype-level analysis, and future work should explore applications such as stress detection, genotype discrimination, and longitudinal phenotyping across diverse crops and environments. Nonetheless, the current case study confirms that the proposed system provides accurate and reliable multi-sensor data suitable for plant-level phenotyping, supporting its application in data-driven crop evaluation and breeding programs.

5. Conclusions

This study developed and validated a regulation-compliant, modular multi-sensor UAS platform for high-throughput plant phenotyping using the Inspired Flight IF800 integrated with RGB, multispectral, and thermal sensors. Beyond demonstrating hardware integration, the work establishes a practical open-architecture framework that combines compliant airframe selection, customizable payload design, independent sensor power and control, and a reproducible processing pipeline for extracting plant-level canopy height, coverage, and temperature traits. Field validation in a lantana breeding trial showed that the proposed system can generate accurate and co-registered multi-modal datasets suitable for phenotyping applications. Multispectral- and RGB-derived canopy height estimates showed strong agreement with ground measurements, canopy coverage estimates were highly consistent across segmentation approaches, and calibrated thermal orthomosaics provided reliable canopy temperature estimates for plant-level analysis. These results confirm that a regulation-compliant UAV platform can achieve the accuracy and functional flexibility required for quantitative phenotyping. Overall, this work presents a practical, reproducible, and adaptable solution to restricted or closed commercial UAV ecosystems for agricultural remote sensing and high-throughput phenotyping. The proposed platform offers a practical path toward sustainable, upgradeable, and cost-conscious multi-sensor phenotyping infrastructure for publicly funded agricultural research. Future work should expand validation across additional crops, environments, and payload configurations to further assess transferability and long-term utility.

Supplementary Materials: The following supporting information can be downloaded at: https://www.mdpi.com/article/10.3390/drones10050372/s1, Engineering design files for the custom payload integration system are available at Zenodo (https://zenodo.org/records/19011517, accessed on 12 May 2025), including the complete 3D assembly of the dovetail-mounted bracket and raised top platform provided in STEP and SolidWorks (.SLDPRT) formats. Supplementary figures and tables referenced in the manuscript are also archived in the same repository.

Author Contributions: Conceptualization, L.J. and X.W.; methodology, L.J. and X.W.; validation, L.J., H.H. and X.W.; formal analysis, L.J. and X.W.; resources: Z.D. and X.W.; writing—original draft preparation, L.J., X.W., H.H. and Z.D.; writing—review and editing, L.J. and X.W.; visualization, L.J. and X.W.; funding acquisition, X.W. All authors have read and agreed to the published version of the manuscript.

Funding: This research was supported by the Launching Innovative Faculty Teams in AI (LIFT AI) program at the University of Florida IFAS.

Data Availability Statement: The datasets generated and analyzed during this study are available upon reasonable request. Available materials include: (i) aerial imagery, consisting of processed georeferenced orthomosaics derived from RGB (LUMIX DMC-LX10), multispectral (MicaSense RedEdge-P), and thermal (ICI 8640P) sensors; and (ii) processing documentation, including implementation parameters used in the image-processing pipeline (e.g., HSV thresholds for RGB vegetation masking and OSAVI- and DEM-based thresholds for multispectral–structural segmentation).

Acknowledgments: We sincerely thank William Haxton, a previous undergraduate research assistant in the Phenomics Lab, for his initial design of the UAV payload parts. During the preparation of this manuscript/study, the authors used generative AI tools for the improvement of the expression and grammar. The authors have reviewed and edited the output and take full responsibility for the content of this publication.

Conflicts of Interest: The authors declare no conflicts of interest. The funders had no role in the design of the study; in the collection, analyses, or interpretation of data; in the writing of the manuscript; or in the decision to publish the results.

Abbreviations

The following abbreviations are used in this manuscript:

UAVs	Unmanned Aerial Vehicles
UAS	Unmanned Aerial System
DEM	Digital Elevation Model
DSM	Digital Surface Model
DTM	Digital Terrain Model
GCP	Ground Control Point
GNSS	Global Navigation Satellite System

GSD	Ground Sampling Distance
DLS	Downwelling Light Sensor
OSAVI	Optimized Soil-Adjusted Vegetation Index
HSV	Hue–Saturation–Value
RMSE	Root Mean Square Error
MAE	Mean Absolute Error
OLS	Ordinary Least Squares
LWIR	Long-Wave Infrared
FOV	Field of View
LiPo	Lithium Polymer Battery

References

1. Jones, S.E.; Ayanlade, T.T.; Fallen, B.; Jubery, T.Z.; Singh, A.; Ganapathysubramanian, B.; Sarkar, S.; Singh, A.K. Multi-sensor and multi-temporal high-throughput phenotyping for monitoring and early detection of water-limiting stress in soybean. *Plant Phenome J.* **2024**, *7*, e70009. [CrossRef]
2. Xu, S.; Xu, X.; Zhu, Q.; Meng, Y.; Yang, G.; Feng, H.; Yang, M.; Zhu, Q.; Xue, H.; Wang, B. Monitoring leaf nitrogen content in rice based on information fusion of multi-sensor imagery from UAV. *Precis. Agric.* **2023**, *24*, 2327–2349. [CrossRef]
3. Zhu, S.; Cui, N.; Jin, H.; Jin, X.; Guo, L.; Jiang, S.; Wu, Z.; Lv, M.; Chen, F.; Liu, Q.; et al. Optimization of multi-dimensional indices for kiwifruit orchard soil moisture content estimation using UAV and ground multi-sensors. *Agric. Water Manag.* **2024**, *294*, 108705. [CrossRef]
4. Khan, M.N.; Rahi, A.; Hasan, M.A.; Anwar, S. Decision-Level Multi-Sensor Fusion to Improve Limitations of Single-Camera-Based CNN Classification in Precision Farming: Application in Weed Detection. *Computation* **2025**, *13*, 174. [CrossRef]
5. Li, Y.; Zhao, B.; Wang, J.; Li, Y.; Yuan, Y. Winter Wheat Yield Estimation Based on Multi-Temporal and Multi-Sensor Remote Sensing Data Fusion. *Agriculture* **2023**, *13*, 2190. [CrossRef]
6. Zhu, H.; Liang, S.; Lin, C.; He, Y.; Xu, J.-L. Using Multi-Sensor Data Fusion Techniques and Machine Learning Algorithms for Improving UAV-Based Yield Prediction of Oilseed Rape. *Drones* **2024**, *8*, 642. [CrossRef]
7. Fei, S.; Hassan, M.A.; Xiao, Y.; Su, X.; Chen, Z.; Cheng, Q.; Duan, F.; Chen, R.; Ma, Y. UAV-based multi-sensor data fusion and machine learning algorithm for yield prediction in wheat. *Precis. Agric.* **2023**, *24*, 187–212. [CrossRef] [PubMed]
8. Herrero-Huerta, M.; Rodriguez-Gonzalvez, P.; Rainey, K.M. Yield prediction by machine learning from UAS-based multi-sensor data fusion in soybean. *Plant Methods* **2020**, *16*, 78. [CrossRef]
9. Ravi, R.; Hasheminasab, S.M.; Zhou, T.; Masjedi, A.; Quijano, K.; Flatt, J.E.; Crawford, M.; Habib, A. *UAV-Based Multi-Sensor Multi-Platform Integration for High Throughput Phenotyping*; SPIE: Bellingham, WA, USA, 2019; Volume 11008.
10. Samaras, S.; Diamantidou, E.; Ataloglou, D.; Sakellariou, N.; Vafeiadis, A.; Magoulianitis, V.; Lalas, A.; Dimou, A.; Zarpalas, D.; Votis, K.; et al. Deep Learning on Multi Sensor Data for Counter UAV Applications—A Systematic Review. *Sensors* **2019**, *19*, 4837. [CrossRef]
11. Maes, W.H.; Steppe, K. Perspectives for Remote Sensing with Unmanned Aerial Vehicles in Precision Agriculture. *Trends Plant Sci.* **2019**, *24*, 152–164. [CrossRef]
12. Feng, A.; Zhou, J.; Vories, E.D.; Sudduth, K.A.; Zhang, M. Yield estimation in cotton using UAV-based multi-sensor imagery. *Biosyst. Eng.* **2020**, *193*, 101–114. [CrossRef]
13. Lee, D.-H.; Park, J.-H. Development of a UAS-Based Multi-Sensor Deep Learning Model for Predicting Napa Cabbage Fresh Weight and Determining Optimal Harvest Time. *Remote Sens.* **2024**, *16*, 3455. [CrossRef]
14. Pádua, L.; Adão, T.; Sousa, A.; Peres, E.; Sousa, J.J. Individual Grapevine Analysis in a Multi-Temporal Context Using UAV-Based Multi-Sensor Imagery. *Remote Sens.* **2020**, *12*, 139. [CrossRef]
15. Wang, Q.; Che, Y.; Shao, K.; Zhu, J.; Wang, R.; Sui, Y.; Guo, Y.; Li, B.; Meng, L.; Ma, Y. Estimation of sugar content in sugar beet root based on UAV multi-sensor data. *Comput. Electron. Agric.* **2022**, *203*, 107433. [CrossRef]
16. Xu, R.; Li, C.; Bernardes, S. Development and Testing of a UAV-Based Multi-Sensor System for Plant Phenotyping and Precision Agriculture. *Remote Sens.* **2021**, *13*, 3517. [CrossRef]
17. Yu, T.; Zhou, J.; Fan, J.; Wang, Y.; Zhang, Z. Potato Leaf Area Index Estimation Using Multi-Sensor Unmanned Aerial Vehicle (UAV) Imagery and Machine Learning. *Remote Sens.* **2023**, *15*, 4108. [CrossRef]
18. U.S. House of Representatives. Rules Committee Print 118-52: Text of the House Amendment to the Senate Amendment to H.R. 5009; Section 1709 of the National Defense Authorization Act (NDAA). Available online: https://www.congress.gov/committee-print/118th-congress/house-committee-print/57838 (accessed on 15 September 2025).
19. Florida Senate. Section 934.50–Search and Seizure Using a Drone. Available online: https://www.flsenate.gov/laws/statutes/2021/934.50 (accessed on 15 September 2025).

20. Florida Department of Management Services. Rule 60GG-2.0075–Drone Operations. Available online: https://www.flrules.org/gateway/ruleno.asp?id=60GG-2.0075 (accessed on 15 September 2025).
21. Salinas, J.C.; Lewandowski, T. Blue Unmanned Aircraft Systems Explained: The Current Drone Market, Flight Regulations, and Debunking Common Misconceptions. *Transp. Res. Rec.* **2025**, *2679*, 1802–1813. [CrossRef]
22. Gang, M.S.; Sutthanonkul, T.; Lee, W.S.; Liu, S.; Kim, H.J. Estimation of Strawberry Canopy Volume in Unmanned Aerial Vehicle RGB Imagery Using an Object Detection-Based Convolutional Neural Network. *Sensors* **2024**, *24*, 6920. [CrossRef]
23. Argento, F.; Merz, Q.; Perich, G.; Anken, T.; Walter, A.; Liebisch, F. A comparison of proximal and remote optical sensor platforms for N status estimation in winter wheat. *Comput. Electron. Agric.* **2025**, *232*, 110110. [CrossRef]
24. Defense Innovation Unit. Blue UAS Cleared List. Available online: https://www.diu.mil/blue-uas-cleared-list (accessed on 15 September 2025).
25. Ji, L.; Wang, X.; Elwakil, W. Selected UAV Options for Agricultural Imaging and Mapping Applications under Florida's UAS Regulations: AE613, 11/2025. *EDIS* **2025**. [CrossRef]
26. GRYFN. Multi-Modal Sensing Solutions. Available online: https://www.gryfn.io/ (accessed on 15 September 2025).
27. University of Florida IFAS Extension. Florida Soil. Available online: https://gardeningsolutions.ifas.ufl.edu/care/planting/florida-soil/ (accessed on 17 April 2026).
28. Wang, X.; Silva, P.; Bello, N.M.; Singh, D.; Evers, B.; Mondal, S.; Espinosa, F.P.; Singh, R.P.; Poland, J. Improved Accuracy of High-Throughput Phenotyping From Unmanned Aerial Systems by Extracting Traits Directly From Orthorectified Images. *Front. Plant Sci.* **2020**, *11*, 587093. [CrossRef] [PubMed]
29. Rondeaux, G.; Steven, M.; Baret, F. Optimization of soil-adjusted vegetation indices. *Remote Sens. Environ.* **1996**, *55*, 95–107. [CrossRef]
30. Wang, H.; Song, M. Ckmeans.1d.dp: Optimal k-means Clustering in One Dimension by Dynamic Programming. *R J.* **2011**, *3*, 29–33. [CrossRef] [PubMed]
31. Belwalkar, A.; Poblete, T.; Zarco-Tejada, P. Airborne Subnanometer Hyperspectral Imaging Reveals Early Biotic-Stress Symptoms via Fraunhofer Lines. *IEEE Geosci. Remote Sens. Lett.* **2026**, *23*, 5503605. [CrossRef]